

This is an Open Access document downloaded from ORCA, Cardiff University's institutional repository: <https://orca.cardiff.ac.uk/id/eprint/167923/>

This is the author's version of a work that was submitted to / accepted for publication.

Citation for final published version:

Lin, Changzheng, Chen, Xin, Wang, Ling, Li, Weijia, Wang, Zhenyu, Li, Mingtao, Feng, Jiangtao, Hou, Bo and Yan, Wei 2024. Electrocatalytic conversion of nitrate into ammonia through heterogeneous catalysis of NiMoO₄ and Cu/Cu₂O. *Advanced Functional Materials* 34 (36), 2401287. 10.1002/adfm.202401287

Publishers page: <http://dx.doi.org/10.1002/adfm.202401287>

Please note:

Changes made as a result of publishing processes such as copy-editing, formatting and page numbers may not be reflected in this version. For the definitive version of this publication, please refer to the published source. You are advised to consult the publisher's version if you wish to cite this paper.

This version is being made available in accordance with publisher policies. See <http://orca.cf.ac.uk/policies.html> for usage policies. Copyright and moral rights for publications made available in ORCA are retained by the copyright holders.



**Electrocatalytic Conversion of Nitrate into Ammonia through
Heterogeneous Catalysis of NiMoO₄ and Cu/Cu₂O**

Changzheng Lin, Xin Chen, Ling Wang, Weijia Li, Zhenyu Wang, Mingtao Li, Jiangtao Feng, Bo Hou*, Wei Yan**

C. Lin, X. Chen, L. Wang, W. Li, Z. Wang, J. Feng, W. Yan

Department of Environmental Science & Engineering, School of Energy and Power Engineering, Xi'an Jiaotong University, 28 Xianning West Road, Xi'an, 710049, China
E-mail: fjtes@xjtu.edu.cn (Jiangtao Feng)

B. Hou

School of Physics and Astronomy, Cardiff University, The Parade, Cardiff, CF24 3AA, Wales, UK.

E-mail: HouB6@cardiff.ac.uk (Bo Hou)

W. Yan

State Key Laboratory of Multiphase Flow in Power Engineering, School of Energy and Power Engineering, Xi'an Jiaotong University, 28 Xianning West Road, Xi'an 710049, China.
E-mail: yanwei@xjtu.edu.cn (Wei Yan)

M. Li

International Research Center for Renewable Energy (IRCRE), State Key Laboratory of Multiphase Flow in Power Engineering (MFPE), Xi'an Jiaotong University, 28 Xianning West Road, Xi'an, Xi'an 710049, China.

Abstract: Facilitating equilibrium in the nitrogen cycle, electrochemical nitrate reduction (NitRR) to ammonia stands as a carbon-free method for ammonia synthesis. Copper-based catalysts, renowned for NitRR, face a hurdle in supplying sufficient hydrogen radicals (*H) for efficient hydrogenation of NitRR intermediates. Addressing this, we leverage NiMoO₄ as an excellent *H donor, synergistically coupling it with a copper-based catalyst. Our work introduces a high-performance NiMoO₄/CuO nanowire (NW)/Copper foam (CF) catalyst for NitRR, achieving a remarkable Faraday efficiency (FE) of 98.8% and a yield of 0.8221 mmol cm⁻² h⁻¹. Operating at -0.2 V versus reversible hydrogen electrode (*vs.* RHE) in an H-type electrolytic cell, the catalyst demonstrates exceptional stability over 20 hours. Additionally, coupling NitRR with an air stripping process enables efficient collection of NH₄Cl products, offering a practical avenue for converting waste nitrates into valuable ammonia products. In-depth in-situ electrochemistry and density-functional theory (DFT) calculations affirm the transformation of CuO into Cu/Cu₂O during the electrocatalytic reduction process. Cu/Cu₂O catalyzes nitrate conversion to nitrite, while NiMoO₄, serving as a *H donor, facilitates deoxidation and hydrogenation of other N intermediates on the Cu/Cu₂O surface, effectively driving the reduction of nitrate to ammonia.

Keywords: Electrochemical nitrate reduction to ammonia, CuO nanowire, In-situ electrochemical reduction, Heterogeneous catalysis, Density-functional theory

1. Introduction

Ammonia (NH_3), a pivotal raw material in diverse industries such as agricultural, plastic, pharmaceutical, and textile industries, is emerging as a carbon-free energy carrier due to its remarkable energy density (4.32 kW h L^{-1}).^[1-4] The prevailing industrial synthesis of NH_3 heavily relies on the energy-intensive and carbon-emission intensive Haber-Bosch (H-B) process, accounting for 1-2% of global energy consumption and contributing to approximately 1% of energy-related CO_2 emission.^[5-6] The electrocatalytic reduction of nitrogen (N_2) or nitrate (NO_3^-) to ammonia (NH_3), utilizing water as a proton source, has garnered significant attention for its mild reaction conditions and compatibility with renewable energy sources. However, challenges inherent in N_2 , such as its high $\text{N}\equiv\text{N}$ bond strength ($941 \text{ kJ}\cdot\text{mol}^{-1}$) and poor solubility ($0.66 \text{ mmol}\cdot\text{L}^{-1}$ under ambient conditions), result in a relatively low Faraday efficiency (FE) for electrocatalytic N_2 -to- NH_3 conversion ($\text{eN}_2\text{-NH}_3$), with a yield rate two orders of magnitude lower than that of H-B process.^[7-11] To overcome this obstacle, NO_3^- emerge as an ideal nitrogen source due to its prevalence in agricultural and industrial wastewater, exceptional water solubility, and low $\text{N}=\text{O}$ bond energy ($204 \text{ kJ}\cdot\text{mol}^{-1}$).^[7] Consequently, employing NO_3^- as a precursor imparts sustainable characteristics to NH_3 electrosynthesis, presenting an economically viable pathway to address environmental pollution.

Advanced electrodes incorporating precious metals, such as Pt, Pd and Ru, have been developed as electrocatalysts for the electrochemical nitrate reduction reaction (NitRR) to ammonia electrocatalysts.^[12-16] Despite their efficacy, the widespread application of these electrodes is hindered by their high cost and limited availability. Recent development in electrocatalysts have shifted towards Earth's abundant transition metals, aiming to address the inherent limitations of noble metal-based counterparts.^[17-18] However, NitRR utilizing transition metal electrocatalysts often exhibits compromised selectivity and catalytic efficiency due to the weak affinity towards NO_3^- and competition with hydrogen evolution reaction (HER). It is noteworthy that the comparable energy levels of Cu's d orbital and the lowest unoccupied molecular orbital (LUMO) π^* molecular orbital of NO_3^- contribute to an exceptional binding energy, inhibiting HER while promoting the catalysis of NO_3^- to NO_2^- , a rate-determining step of NitRR.^[19-21] The robust adsorption and deactivation of NitRR intermediates ($^*\text{NO}_3$, $^*\text{NO}_2$, $^*\text{NO}$, $^*\text{N}$, $^*\text{NH}$ and $^*\text{NH}_2$) on Cu-based electrocatalysts hinder the electrochemical reduction to ammonia, emphasizing the need for a tailored approach.^[22-23] In comparison to nickel foam or carbon-based substrates such as carbon paper or carbon cloth, copper foam (CF) presents a promising alternative. By adjusting the surface topography and valence state, CF provides more

active NitRR sites, serving as an efficient electrical conductor and reducing substrate material costs.^[24-30]

To overcome the issue of nitrate reduction intermediates becoming inactive on the surface of Cu-based catalysts, hydrogen radicals (*H), known for their exceptional reducing properties, can effectively facilitate the conversion of nitrite into ammonia. To date, most catalysts that facilitate the generation of hydrogen radicals from water have relied on precious metals (RuO_x/Pd^[31], Ru-ST^[32], Au/Cu^[33], RuCu^[12], RuCo_x^[16]). However, the widespread application of these catalysts is impeded by their high cost and limited availability. Serving as an *H donor, NiMoO₄, acting as a HER inert catalyst, inhibits the Heyrovsky reaction (*H_{ads}+H₂O+e⁻→H₂+OH⁻) and activates the Volmer reaction (H₂O+e⁻→*H_{ads}+OH⁻).^[34] This dual functionality makes NiMoO₄ an attractive alternative, as it overcomes the limitations associated with weak nitrogen intermediates adsorption and the need for high potentials in NitRR reactions. Despite its underexplored application in NitRR, the synergistic combination of a heterogeneous Cu-based catalyst, known for its excellent nitrogen intermediate adsorption properties, with NiMoO₄, exhibiting exceptional hydrogen adsorption performance, holds promise in enhancing catalytic efficiency while concurrently reducing costs.

In this study, we synthesized NiMoO₄/CuO nanowire(NW)/CF through sequential chemical oxidation and hydrothermal methods for NitRR. Encouragingly, NiMoO₄/CuO NW/CF exhibited excellent ammonia generation activity (0.8221 mmol cm⁻² h⁻¹) and Faraday efficiency (FE) (98.8%) at an ultra-low potential of -0.2 V versus reversible hydrogen electrode (*vs.* RHE), outperforming the conventional Cu catalysts. Our experimental findings elucidate the distinct roles of NiMoO₄ and Cu₂O (CuO reduction product) in the reduction of NO₃⁻ to NO₂⁻ and NO₂⁻ to NH₃ respectively, underscoring their cooperative heterogeneous catalysis on NiMoO₄/CuO NW/CF catalysts with high NH₃ product rate and FE. Density-functional theory (DFT) calculations indicate that Cu₂O facilitates the rate control step (NO₃⁻ reduced to NO₂⁻) of NitRR. However, its performance in the intermediates' conversion from NO₂⁻ to NH₃ is suboptimal. In contrast, NiMoO₄ catalytic decomposition of water into hydrogen radicals proves excellent, effectively promoting intermediate catalysis and facilitating the electrocatalytic process involving multi-electron multi-step reactions.

2. Results and Discussion

2.1. Catalyst design and characterization.

The synthesis of NiMoO₄/CuO NW/CF catalysts is schematically illustrated in **Figure 1a**. CuO NW/CF was obtained by calcination of Cu(OH)₂ NW/CF, which was synthesized on a

copper foam substrate using chemical oxidation method. The hydrothermal method was employed to synthesize NiMoO₄ nanosheets and nanospheres on the surface of CuO NW/CF substrates, to obtain NiMoO₄/CuO NW/CF.

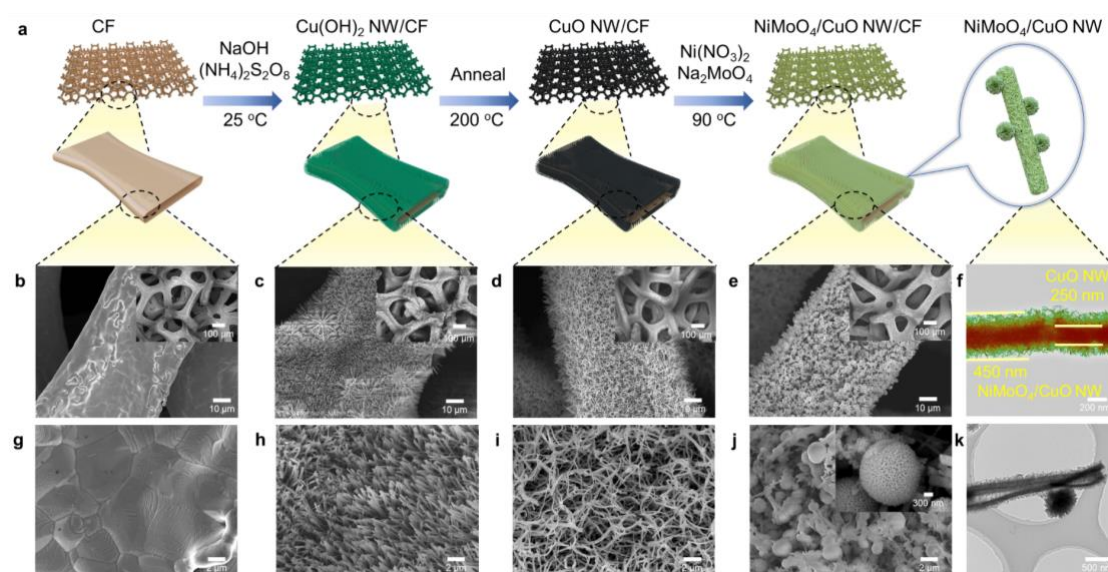


Figure 1 Structural characterizations of catalysts. (a) Schematic illustration of the preparation of a NiMoO₄/CuO NW/CF binary cooperative catalyst. SEM images of the CF (b, g), Cu(OH)₂ NW/CF (c, h), CuO NW/CF (d, i) and NiMoO₄/CuO NW/CF (e, j). Typical TEM image of NiMoO₄/CuO NW/CF (f, k).

Scanning electron microscopy (SEM) images show the morphological change from CF to NiMoO₄/CuO NW/CF. Cu(OH)₂ NW/CF electrode demonstrates a densely packed and uniformly distributed arrangement of Cu(OH)₂ nanowires (Figure 1c, h), contrasting with the sleek surface of bare CF (Figure 1b, g). The Cu(OH)₂ NW/CF was subjected to calcination, resulting in the formation of CuO NW/CF with a disordered nanowire morphology (Figure 1d, i). The nitrogen adsorption and desorption isotherms revealed that CuO NW exhibited a significantly higher specific surface area compared with CF (Figure S1). The SEM image in Figure 1e, j illustrates a typical NiMoO₄/CuO NW/CF composite, with the nanowire exhibiting a length of approximately 12 μm (Figure S2). The vertical orientation of the CuO NW is supported by the CF substrate, while NiMoO₄ nanosheets and nanoflowers grew vertically on its surface features. To acquire more comprehensive structural information, NiMoO₄/CuO NW were extracted from NiMoO₄/CuO NW/CF and subjected to transmission electron microscopy (TEM) analysis. The TEM images in Figure 1f, k reveal the growth of NiMoO₄ on CuO NW (250 nm), resulting in a rough surface with an approximate diameter of 450 nm. Graph element mapping analysis reveals a uniform distribution of Cu and O elements throughout the CF (The surface is partially oxidized), Cu(OH)₂ NW/CF and CuO NW/CF (Figure S3-5). The elements Ni, Mo, Cu, and O distribute within the NiMoO₄/CuO NW/CF, and elemental analysis was

simultaneously conducted on different regions to confirm their distribution and proportion of elements (**Figure S6-7**).

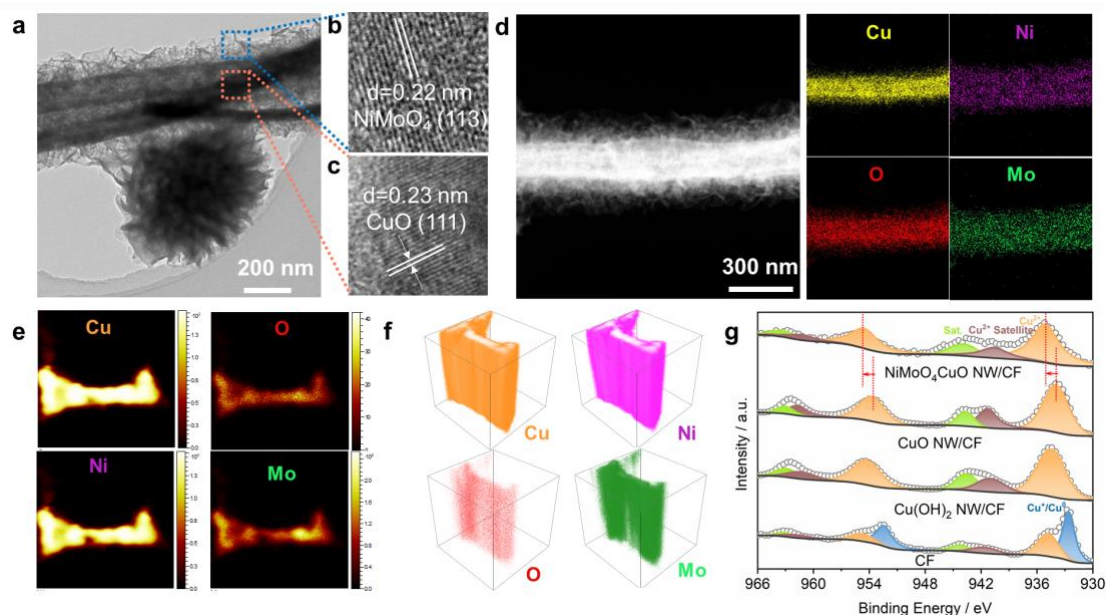


Figure 2 Structural characterizations of catalysts. (a) TEM and (b, c) high-resolution TEM (HRTEM) images of NiMoO₄/CuO NW/CF. (d) TEM element mapping images of NiMoO₄/CuO NW. (e) TOF-SIMS surface mapping of Cu, O, Ni and Mo on NiMoO₄/CuO NW/CF. (f) spatial distributions of Cu, O, Ni and Mo on NiMoO₄/CuO NW/CF detected by TOF-SIMS. (g) Cu 2p XPS spectra of CF, Cu(OH)₂ NW/CF, CuO NW/CF and NiMoO₄/CuO NW/CF.

To gain more detailed structural information, some NiMoO₄/CuO NW were scraped off from the NiMoO₄/CuO NW/CF and subjected to high-resolution transmission electron microscopy (HRTEM) characterization. The TEM image in **Figure 2a** reveals the presence of a rough surface on a nanowire structure with a diameter of approximately 450 nm for NiMoO₄/CuO NW. Additionally, a NiMoO₄ nanoflower measuring approximately 650 nm in diameter is observed to be grown on the surface of the NiMoO₄/CuO NW. The HRTEM image reveals that the d-spacing values of 0.22 nm and 0.23 nm correspond to the (1 1 3) plane of NiMoO₄ and the (1 1 1) plane of CuO, respectively (**Figure 2b-c, S8**).^[34-35] To further analyze the element composition and distribution of NiMoO₄/CuO NW, high-angle annular dark-field scanning transmission electron microscopy (HAADF-STEM) and corresponding element mappings were acquired. As illustrated in **Figure 2d**, the distribution of Cu in the NiMoO₄/CuO NW is primarily observed in the core, while the elements O, Ni, and Mo are evenly distributed throughout the NiMoO₄/CuO NW. Chemical analyses were carried out on the regions of the patterned NiMoO₄/CuO NW/CF surface using time-of-flight secondary ion mass spectrometry (TOF-SIMS), and the 3D render results showed that Cu, O, Ni, and Mo are uniformly distributed in the vertical direction of the CuO NW (**Figure 2e, f**), further supported by Cross-section SEM images and elemental mapping of the NiMoO₄/CuO NW/CF (**Figure S9**). CF,

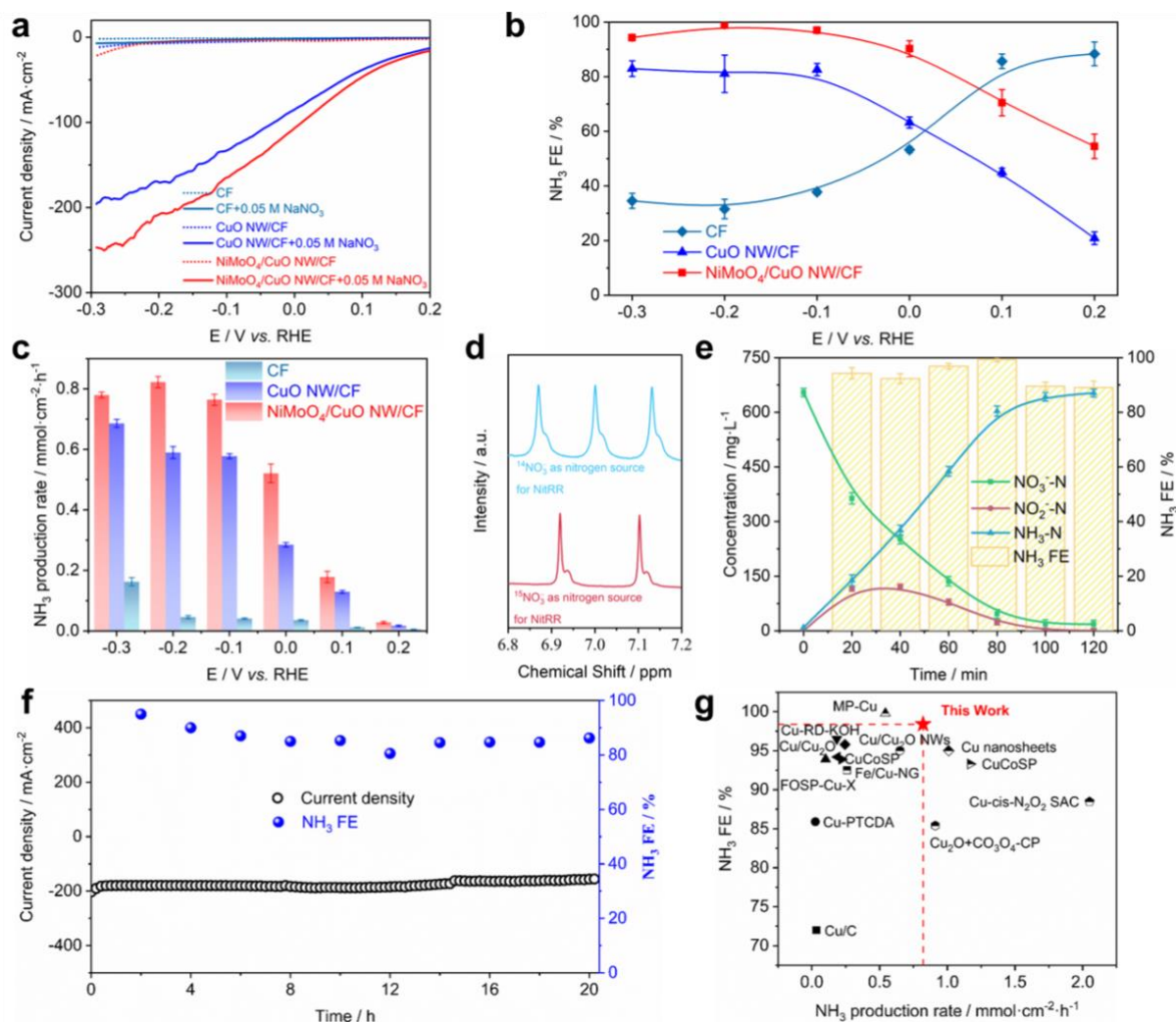
Cu(OH)₂ NW/CF, CuO NW/CF and NiMoO₄/CuO NW/CF were further verified by X-ray diffraction (XRD) patterns (**Figure S10**). The diffraction pattern of CF reveals the presence of three peaks at 43.29, 50.43, and 74.13 degrees, corresponding to the (1 1 1), (2 0 0), and (2 2 0) crystallographic planes for Cu, respectively (JCPDS no.04-0836). The Cu(OH)₂ NW/CF electrodes exhibited additional peaks corresponding to Cu(OH)₂ (JCPDS no.13-0420) in addition to the Cu peak. After calcination, the CuO NW/CF exhibits a peak corresponding to CuO (JCPDS no.45-0937). The presence of NiMoO₄ (JCPDS no.05-0667) is indicated by a peak of 36.49 degree on the NiMoO₄/CuO NW/CF electrode. As shown in **Figure S11**, CF, Cu(OH)₂ NW/CF, CuO NW/CF and NiMoO₄/CuO NW/CF contain Ni, Mo (NiMoO₄/CuO NW/CF), Cu, O, and C peaks without any other impurity. As shown in **Figure 2g**, high resolution X-ray photoelectron spectroscopic (XPS) spectrum of Cu 2p_{3/2} presents peaks at 932.6 and 934.8 eV (and the Cu 2p_{1/2} presents peaks at 954.8 and 952.4 eV), indicating the CF contained both zero valent Cu and oxidation generated Cu²⁺, which corresponds to metal Cu and CuO. The Cu 2p spectra of Cu(OH)₂ NW/CF, CuO NW/CF, and NiMoO₄/CuO NW/CF exhibited prominent peaks at ≈934 eV and ≈954 eV for the Cu 2p_{3/2} and Cu 2p_{1/2} states, respectively, providing evidence that the three electrodes predominantly consisted of Cu²⁺. The peaks of Cu 2p_{3/2} in NiMoO₄/CuO NW/CF slightly shift to higher binding energy compared with that in CuO NW/CF. Such corresponding shifts demonstrate that electron transfers from Cu to Ni and Mo occur in NiMoO₄/CuO hetero-phase interface, which is mainly attributed that Ni (Electronegativity: 1.91 Pauling Scale) and Mo (Electronegativity: 2.16 Pauling Scale) is more electronegative than Cu (Electronegativity: 1.90 Pauling Scale)^[36]. The high-resolution XPS spectra for Mo and Ni are presented in **Figure S12** and **Figure S13**, respectively. The Mo 3d spectrum exhibits peaks at 232.2eV (Mo 3d_{5/2}) and 235.3eV (Mo 3d_{3/2}), indicating the presence of Mo⁶⁺. Similarly, the Ni 2p spectrum shows peaks at 856.8V (Ni 2p_{3/2}) and 874.9eV (Ni 2p_{1/2}), suggesting the existence of Ni²⁺.

2.2. Electrocatalytic NitRR performance.

The electrochemical NitRR performance of the NiMoO₄/CuO NW/CF was investigated under ambient temperature and pressure in a standard three-electrode H-type cell. In this study, NO₃⁻, NO₂⁻ and NH₃ were quantified by ultraviolet-visible (UV-vis) spectrophotometry with calibration curves (**Figure S14**). An industrial wastewater-relevant nitrate concentration of 0.05 M was used in our electrolyte for the standard electrochemical characterizations of the catalysts^[37-38]. Initially, NiMoO₄/CuO NW/CF composites were prepared using different Ni and Mo precursors (0.5:0.5, 1:1, 1.5:15, 2:2 and 2.5:2.5). The results depicted in **Figure S15**

demonstrate that the NiMoO₄/CuO NW/CF composite synthesized with a 1.5 mmol:1.5 mmol ratio of Ni and Mo precursors exhibited superior performance. To emphasize the superiority of NiMoO₄ in modifying CuO NW/CF, we synthesized NiMoO₄ NW on the surface of nickel foam following the methodology described in literature and subsequently conducted CuO modification.^[34] The LSV results (**Figure S16**) indicate that approximately 6.6% of the 174.6 mA current in CuO/NiMoO₄ NW/NF is utilized for electrocatalytic hydrogen evolution at -0.2 V *vs.* RHE, owing to the inherent electrocatalytic activity of NiMoO₄. Consequently, incorporating CuO into NiMoO₄ leads to a reduction in the Faraday efficiency of CuO/NiMoO₄ NW/NF. The three major control samples, CF and CuO NW/CF presented distinct electrocatalytic behaviors compared with that of NiMoO₄/CuO NW/CF. Linear sweep voltammetry (LSV) curves recorded in the electrolyte with or without NO₃⁻ using CF, CuO NW/CF and NiMoO₄/CuO NW/CF working electrode show obvious discrepancy from 0.2 V to -0.3 V *vs.* RHE (**Figure 3a**), suggesting the participation of NO₃⁻ in the electro-reduction process. Furthermore, a series of potentials from 0.2 V to -0.3 V *vs.* RHE were performed to investigate the catalytic properties of CF, CuO NW/CF and NiMoO₄/CuO NW/CF for NitRR. CF showed an early onset of ammonia generation with 88.4% and 85.1% FE at 0.2 V and 0.1 V *vs.* RHE, respectively, which suggests facile NitRR kinetics on the Cu sites. However, within the CF range of 0.2 V to -0.3 V *vs.* RHE, its ammonia yield remains significantly low (**Figure 3b, c**). The CuO NW/CF demonstrated an approximately 80% earlier onset of ammonia production at -0.1 V, indicating favorable kinetics for nitrate reduction to nitrite at the CuO site. However, the FE of CuO NW/CF electrodes in ammonia conversion is limited (**Figure 3b, S17**). This is unsurprising given that CuO is a widely acknowledged active catalyst for the reduction of nitrate to nitrite. However, Cu-based materials exhibit pronounced intermediate adsorption during nitrite reduction to ammonia, consequently leading to a diminished FE of ammonia production. To address this issue, NiMoO₄ is utilized as an exceptional *H donor and loaded onto the surface of CuO NW. The incorporation of NiMoO₄ onto carbon paper (CP) exhibited limited electrocatalytic nitrate properties, thereby highlighting its unique role as a *H donor (**Figure S18**). This approach not only inhibits the FE of nitrite but also enhances the FE of ammonia, with the highest NH₃ FE reaching 98.8%. The NH₃ yield exhibited a “volcano” pattern, initially increasing and then decreasing as the potential decreased. The primary factor contributing to this increase was the rise in NH₃ current with decreasing potential. However, despite further reduction in potential leading to an increase in current density, it also triggered a side reaction of HER, resulting in a decrease in NH₃ yield (**Figure 3c**). The selectivity results for NO₂⁻ and NH₃ at different potentials, as depicted in **Figure S19**, demonstrate that a

remarkable NH_3 selectivity is up to 94.9% at -0.2 V vs. RHE. To identify whether the detected NH_3 is from the NitRR or other impurities in electrocatalysts, isotope tracing experiments are performed by using ^{15}N -labeled $^{15}\text{NO}_3^-$ as a reactant. After changing the reactant to $^{15}\text{NO}_3^-$, the triple ^1H NMR peak for $^{14}\text{NH}_4^+$ alters to a double peak for $^{15}\text{NH}_4^+$ (**Figure 3d**), indicating that the detected NH_3 indeed originates from the NitRR other than impurities.^[39-40]



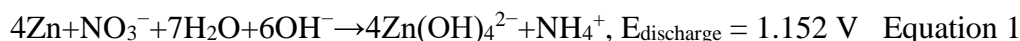
To evaluate NiMoO₄/CuO NW/CF's capability in nitrate removal, we performed a batch conversion test with an initial approximately 0.05 M NO₃⁻ and measured the remaining products (**Figure 3e**). Impressively, nearly all the N sources were converted into NH₃ within

two hours. The overall NH_3 FE remained over 90%. After two hours of electrolysis, NO_3^- and NO_2^- were both significantly reduced below the World Health Organization (WHO) regulations for drinking water.^[41] To further highlight their industrial production potential, a series of experiments were performed. First, electrolytes with different NO_3^- concentrations (0.005~0.1 M) were studied, and the high performance was found to be maintained well over a wide range (**Figure S20**). It is worth noting that the high performance remained good during a continuous 20 h of timed amperometric testing (**Figure 3f**). Indeed, the topography of CuO NW and NiMoO₄ nanoflowers and the XPS of Cu, Ni, and Mo remained virtually unchanged after the electrochemical test, demonstrating its exceptional durability (**Figure S21, S22**). These results unequivocally indicate that NiMoO₄/CuO NW/CF exhibits remarkable electrocatalytic performance towards NitRR. **Figure 3g** compares the nitrate reduction performance of NiMoO₄/CuO NW/CF with that of other electrocatalysts, and the detailed comparison of nitrate reduction performance is summarized in **Table S1**. NiMoO₄/CuO NW/CF exhibits a high FE for NH_3 production at high partial current densities that is superior or comparable to the performance of non-noble metal or alloy catalysts.

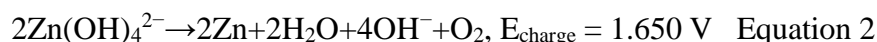
2.3. Rechargeable Zn-Nitrate battery

The schematic diagram of the aqueous rechargeable zinc-nitrate (Zn-NO_3) battery is illustrated in **Figure S23**. In the anode compartment, a mixture solution containing 3 M KOH and 0.02 M $\text{Zn}(\text{CH}_3\text{COO})_2$ was utilized, while the catholyte consisted of 3 M KOH with 0.5 M KNO_3 . An Nafion 1110 membrane was employed to effectively separate the two electrolytes. During discharge, Zn metal on the anode dissolves and releases electrons, facilitating NitRR at the cathode through electron transfer. On charging, water undergoes oxidation to produce O_2 , while $\text{Zn}(\text{OH})_4^{2-}$ is formed at the anode leading to the generation of Zn, thereby resulting in the subsequent battery reaction.

Discharge reaction:



Charge reaction:



Overall reaction:



The constant open circuit potential of NiMoO₄/CuO NW/CF-based Zn-NO₃ battery is 1.15 V vs. Zn/Zn²⁺, as depicted in **Figure 4a**. This value closely aligns with the theoretical voltage of 1.15 V vs. Zn/Zn²⁺ for Zn-NO₃ battery (**Equation 1**). The battery was utilized to power an

electronic timer, and the device operated continuously for 24 hours without any anomalies (**Figure S24**). The discharge curve of the Zn-NO₃ battery in **Figure S25** demonstrates a gradual increase in current density from 2 to 20 mA cm⁻². Initially, the voltage stabilizes at 0.95 V and remains constant for 0.5 hours. Subsequent steps exhibit similar stability, indicating exceptional mass transfer and conductivity.

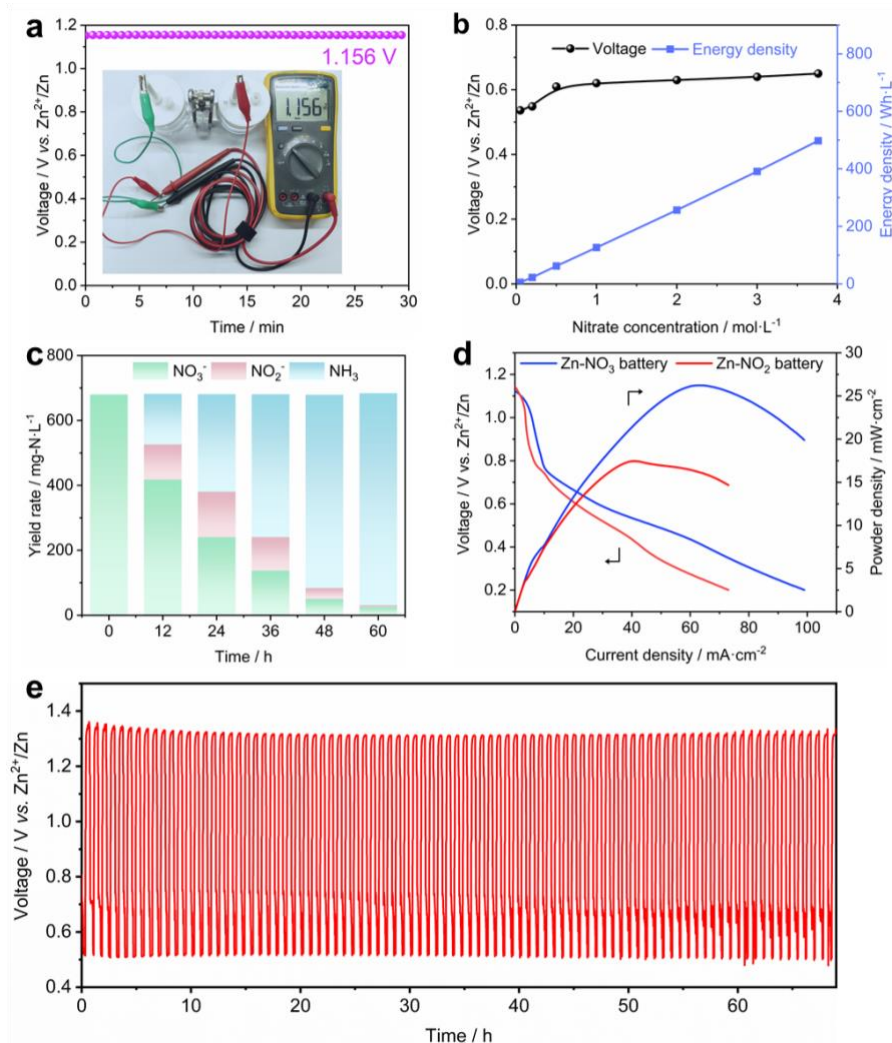


Figure 4 The electrochemical performance of hybrid aqueous Zn-NO₃ battery. (a) Open circuit voltage of Zn-NO₃ battery. (b) Average discharge voltage and corresponding energy density at varying nitrate concentrations. (c) Long-term discharge stability test results for the Zn-NO₃ battery at 20 mA·cm⁻², including the corresponding yield. (d) Discharging polarization curves and corresponding power density curves of the Zn-NO₃ battery. (e) Galvanostatic discharge-charge cycling curves over 90 cycles at 12.5 mA cm⁻².

Ideal Zn-NO₃ batteries in principle show a record high theoretical energy density of 943.2 Wh·L⁻¹ of the catholyte, based on the high solubility of NO₃⁻ in water (38 g/100 mL at 25°C), and that each NO₃⁻ contributes on the cathode side to the storage of eight electrons (that is one electron per 7.7 mass units, i.e. close to metallic Li).^[25] Typically, the voltage of Zn-NO₃ battery stays around 0.70 V at 10 mA·cm⁻², which lowers the calculated energy density to 497.8 Wh·L⁻¹ with 3.76 mol·L⁻¹ of NO₃⁻ in the electrolyte (**Figure 4b**), being still much higher than

that of other aqueous batteries, such as the vanadium flow battery ($25\sim 35 \text{ Wh}\cdot\text{L}^{-1}$), Zn-Br₂ battery ($65 \text{ Wh}\cdot\text{L}^{-1}$), lead battery ($35\sim 45 \text{ Wh}\cdot\text{L}^{-1}$) and Zn-I₂ battery ($166.7 \text{ Wh}\cdot\text{L}^{-1}$).^[42] The conversion of nitrate to ammonia exceeds 95% within a duration of 60 hours, as depicted in **Figure 4c**, under a current density of $20 \text{ mA}\cdot\text{cm}^{-2}$. Furthermore, continuous discharge-charge cycling curves at 12.5 mA cm^{-2} showed good stability and low charge potential of 1.32 V during 90 cycles (**Figure 4e**), which suggests excellent stability of the assembled Zn-NO₃ battery. As a result, the Zn-NO₃ battery reaches a maximal power density of $26.2 \text{ mW}\cdot\text{cm}^{-2}$, superior to the Zn-NO₂ battery with a maximal power density of $17.5 \text{ mW}\cdot\text{cm}^{-2}$ (**Figure 4d**). Importantly, the power density of both types of batteries is higher than recently reported state-of-the-art results using a direct eight-electron transfer process, which further confirms the advantage of our catalyst (**Table S2**).

2.4. Theoretical analysis.

To explain the high NH₃ FE over NiMoO₄/CuO NW/CF compared with CuO NW/CF, we used electrochemical tests, ex-XRD, in-situ Raman and DFT to calculate the minimum energy pathway of the NitRR and HER.

In order to investigate the impact of NiMoO₄ and CuO NW on electrocatalytic activity, we assessed the NitRR and nitrite reducing activities of catalysts (CuO NW/CF and NiMoO₄/carbon paper (CP)) in H-type electrolytic cells. Comparatively, CuO NW/CF exhibited enhanced performance in 1 M KOH solution (with 0.1 M NaNO₃), than that in 1 M KOH solution (with 0.1 M NaNO₂), whereas NiMoO₄/CP demonstrated contrasting behavior (**Figure S26, S27**). The experimental results demonstrate that CuO NW and NiMoO₄ possess excellent catalytic activity towards NO₃⁻-NO₂⁻ and NO₂⁻-NH₃ respectively. After pre-reducing the CF and CuO NW/CF at -0.2 V vs. RHE for 30 minutes, and immersing the pre-reduced electrode in an electrolyte solution (1 M KOH and 0.05 M NaNO₃), the nitrate was converted into nitrite by CuO NW/CF, while a similar phenomenon did not occur in CF. This indicates that there is a spontaneous redox reaction between CuO or its reduction product and NO₃⁻, resulting in the generation of NO₂⁻ (**Figure 5a**). In order to elucidate the mechanism underlying the reduction of NO₃⁻ to NO₂⁻, ex-situ XRD tests were performed on NiMoO₄/CuO NW/CF following pre-reduction. The experimental findings demonstrated that during open circuit potential (OCP) conditions, alongside the presence of a Cu peak, an additional signal indicative of CuO was observed. In addition, in the ex-situ XRD test, we observed that NiMoO₄ had a weak crystal structure due to electrochemical reduction in alkaline solution, and the peaks gradually disappeared. Upon gradual reduction in potential from 0.2 V down to 0 V vs. RHE,

there was a decline in intensity for the CuO signal until its mostly disappearance; concurrently at the potential (0 V vs. RHE), the distinct feature associated with Cu₂O became evident. Moreover, as further decrease in potential occurred from 0 V towards -0.3 V vs. RHE range, there was a progressive enhancement observed for the intensity of this newly formed Cu₂O signal (**Figure 5b, S28**). A similar experimental phenomenon was also observed for CuO NW/CF (**Figure S29**). The pre-reduced CuO NW/CF were immersed in a 1M KOH (0.05M NaNO₃) solution, resulting in the formation of reduced Cu₂O. This pre-reduction process not only enhanced the original peak but also led to the appearance of a new Cu₂O peak. Interestingly, a similar phenomenon was observed when using only 1 M KOH as the reducing solution (**Figure 5c, S30**). The pre-reduced CuO NW/CF electrode was immersed in a 0.05M NaNO₃ solution, subjected to vacuum drying, and subsequently underwent ultrasonic stripping in an ethanol solution. XRD analysis confirmed the presence of CuO, Cu₂O and Cu on the nanowire structure (**Figure S31**). These experimental results indicate that the surface of CuO NW is reduced to Cu and Cu₂O, while spontaneous redox reaction of NO₃⁻ by Cu/Cu₂O leads to the formation of NO₂⁻. Additionally, Cu/Cu₂O is oxidized to Cu₂O and subsequently electrochemically reduced back into Cu/Cu₂O. To gain a more comprehensive understanding of the impact of NiMoO₄ loading on the hydrogenation process, electron paramagnetic resonance (EPR) measurements and cyclic voltammetry (CV) tests were conducted to investigate the generation and transfer of hydrogen radicals (*H). Interestingly, EPR(**Figure 5d**) results revealed that during water electrolysis with CuO NW/CF, a very small amount of *H was produced in the solution, accompanied by a decrease in peak intensity for CuO NW/CF when NO₃⁻ was introduced. Conversely, when NiMoO₄ was loaded onto CuO NW/CF, the peak intensity surpassed that of CuO NW/CF without NO₃⁻. Even after adding NO₃⁻, the peak intensity of NiMoO₄/CuO NW/CF still exhibited a certain degree compared to CuO NW/CF alone, thus demonstrating that NiMoO₄ loading enhances *H supply capacity.^[43] The CVs curve presented in **Figure S32** also demonstrates the oxidation peak of *H, while NiMoO₄/CuO NW/CF exhibits a significantly higher oxidation peak compared with CuO NW/CF.^[44-45] In **Figure S33**, it can be seen that the presence of nitrate significantly diminishes the intensity of the associated *H peak, thereby indicating the involvement of *H in the NitRR reaction. To verify the critical role of *H in the electrochemical systems, tertiary butanol (TBA, 25 mmol/L), a specific *H quencher, was added before electrolysis. NO₃⁻ and NO₂⁻ removal efficiency decreased in the presence of TBA as it hinders *H from reducing NO₃⁻ and NO₂⁻.^[45] The NiMoO₄/CuO NW/CF catalyst exhibited a reduction effect on the 1 M KOH (with NO₃⁻ or NO₂⁻) solution, resulting in a decrease in the rate constant from 2.59 h⁻¹ to 0.93 h⁻¹ and 16.73

h^{-1} to 1.67 h^{-1} upon addition of TBA to the 1M KOH (with NO_3^-) solution, to the 1M KOH (with NO_2^-) solution, respectively. The rate constant for the reduction of NO_2^- to NH_3 decreases by approximately one order of magnitude, providing evidence for the crucial role played by $^*\text{H}$ as reactive intermediate in the process of NO_2^- reduction to NH_3 . (**Figure 5e**). Electrocatalytic NO_3^- to NH_3 conversion proceeds at reduction potentials, at which $\text{NiMoO}_4/\text{CuO}$ NW/CF catalysts suffer from potential-dependent phase reconstruction, leading to the formation of the multi-intermediate phase.

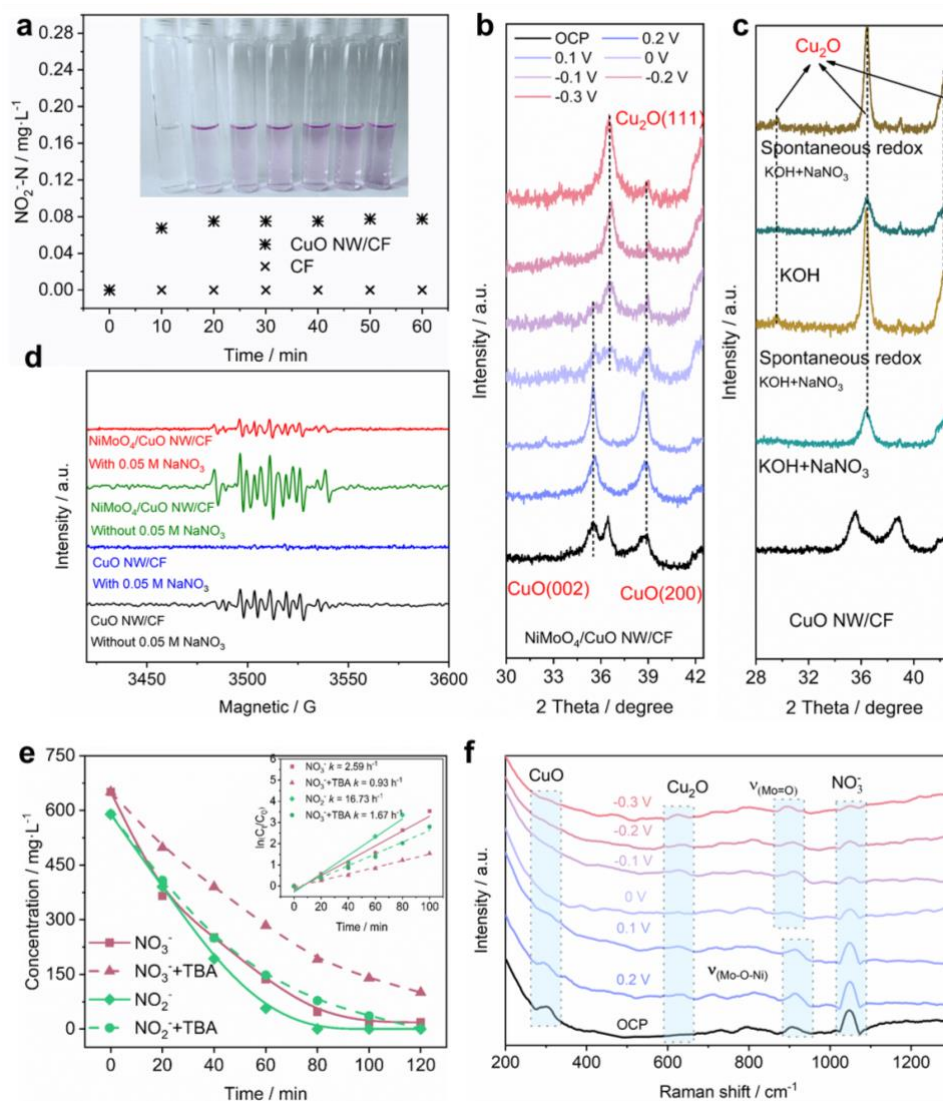


Figure 5 Mechanistic studies for the $\text{NiMoO}_4/\text{CuO}$ NW/CF. (a) Variation in concentration of NO_2^- in the electrolyte after the redox reaction with CuO NW/CF and CF for different times, without an applied potential (illustration: Digital photograph of the electrolyte pre-reduction with CuO NW/CF followed by subsequent addition of nitrite reagent). (b) Ex-situ XRD spectra of the $\text{NiMoO}_4/\text{CuO}$ NW/CF catalyst at different applied potentials in 1 M KOH electrolyte with 0.05 M NaNO_3 . (c) XRD of CuO NW/CF after pre-reduction and autocatalysis. (d) Electrochemical quasi in situ EPR tests at -0.2 V vs. RHE. (e) Under TBA masking conditions, the $\text{NiMoO}_4/\text{CuO}$ NW/CF electrode exhibited a NO_3^- change over time and its rate constant in a -0.2 V vs. RHE, 1 M KOH (0.05 M NaNO_3 or NaNO_2) solution. (f) In-situ Raman spectra of the $\text{NiMoO}_4/\text{CuO}$ NW/CF at different applied potentials in 1 M KOH electrolyte with 0.05 M NaNO_3 .

In-situ Raman spectroscopy was utilized to monitor the self-reconstruction behavior of the pre-synthesized NiMoO₄/CuO NW/CF catalysts during this process (**Figure S34**). The nitrate reduction test involved the addition of KOH and NaNO₃ was used as the electrolyte. In-situ Raman spectra of the NiMoO₄/CuO NW/CF catalyst at different potentials (**Figure 5f**) revealed that the initial characteristic peak associated with CuO appeared at 298 cm⁻¹ and remained detectable even at a low potential of 0.1 V *vs.* RHE relative to RHE. At 0 V *vs.* RHE, the presence of CuO gradually diminished while a distinct peak corresponding to Cu₂O emerged at 630 cm⁻¹,^[46] consistent with ex-situ XRD analysis mentioned earlier. The simultaneous observation of a Mo-O-Ni Raman peak at approximately 913 cm⁻¹ and its shift towards 890 cm⁻¹ with decreasing potential indicates the formation of Mo-O.^[47-48] The peak observed at 1050 cm⁻¹ corresponds to NO₃⁻, showing relatively higher intensity at higher potentials;^[49] however, as the potential continued to decrease, continuous reduction in NO₃⁻ occurred along with a subsequent decrease in its peak intensity.

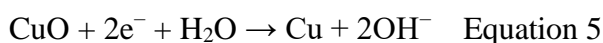
To elucidate the exceptional performance of NiMoO₄ and Cu/Cu₂O, DFT calculations were conducted to investigate the intrinsic impact of various reaction mechanisms involving Cu and Mo. The findings of the aforementioned study indicate that CuO undergoes reduction to form Cu/Cu₂O during the NitRR process, thus highlighting the utilization of Cu/CuO and Cu/Cu₂O as the primary computational material, while calculating NiMoO₄ as a hydrogen radical source for catalytic water splitting.

The work function of a surface is a significant criterion to investigate the surface activity. The work functions of the Cu/CuO (0 0 2) and Cu/Cu₂O (1 1 1) surfaces were calculated based on the following equation 4^[35]:

$$\Phi = E_{VAC} - E_{fermi} \quad \text{Equation 4}$$

where E_{fermi} is the Fermi energy, and E_{VAC} is the electrostatic potential of the vacuum level. The work functions of the Cu/CuO (0 0 2) and Cu/Cu₂O (1 1 1) surface were 7.00 eV (**Figure S35**) and 4.81 eV (**Figure 6a**), respectively. Comparing the work functions of the Cu/CuO (0 0 2) and Cu/Cu₂O (1 1 1) surface, electrons are more likely to overflow from the Cu/Cu₂O (1 1 1) surface, which is more active than the Cu/CuO (0 0 2) surface. Thus, Cu/Cu₂O (1 1 1) is more conducive to the initial *NO₃ adsorption.^[35] Moreover, the charge density difference calculation results for NO₃⁻ before and after adsorption at the Cu/Cu₂O (1 1 1) interface (*Cu/Cu₂O (1 1 1)) (**Figure 6b**) reveal a transfer of oxygen atoms from NO₃⁻ to the Cu position at the Cu/Cu₂O (1 1 1) interface, providing strong evidence for enhanced interaction between *NO₃ and regions of the Cu/Cu₂O (1 1 1) interface.^[50-51] The energy of the HER was computed,

and a comparative analysis of the Faraday efficiency difference between Cu/Cu₂O and NiMoO₄ was conducted. It was observed that the adsorption free energy of NiMoO₄ for H₂O was 1.56 eV, which significantly exceeded that of Cu₂O (0.1 eV). Additionally, the H₂ formation barrier on NiMoO₄ was found to be 1.45 eV, also significantly higher than that of Cu₂O (0.66 eV). This led to an enhanced *H generation and consequently resulted in superior faraday efficiency (**Figure 6c**).^[24] We first calculated the free energy pathway of NitRR to reveal the catalytic mechanism of the two facets. The overall NitRR pathway on the catalyst surface is shown in **Figure 6d** and the related structures of intermediates are shown in **Figure S36**. The pathway includes the adsorption of NO₃⁻ to form *NO₃, deoxygenation of the N species, hydrogenation of the N species, and desorption of the reduced species. It is clear that the Gibbs adsorption energy (G_{ads}) of *NO₃ on Cu/Cu₂O (1 1 1) is -2.33 eV, lower than that of Cu/CuO (0 0 2) (-2.3 eV), suggesting that the Cu/Cu₂O (1 1 1) facet triggers the reaction. The adsorption energy of other intermediates (*NO₂, *NO, *N, *NH, *NH₂, *NH₃) on the Cu/CuO (0 0 2) surface is lower compared with that of Cu/Cu₂O (1 1 1). However, previous studies^[22] have indicated that the catalyst's robust adsorption of NitRR intermediates (*NO₂, *NO, *N, *NH, *NH₂, *NH₃) often leads to rapid deactivation, thereby impeding subsequent electrochemical reduction into NH₃. In addition, the NH₃ desorption step (*NH₃+e⁻→NH₃) from Cu/CuO (0 0 2) exhibits a higher uphill ΔG of 2.65 eV compared to the same reaction step of NH₃ desorption from Cu/Cu₂O (1 1 1) which only requires 0.3 eV. The aforementioned analysis results indicate that in NO₃⁻ adsorption, intermediate adsorption, and NH₃ desorption processes on Cu/Cu₂O (1 1 1) outperforms that of Cu/CuO (0 0 2). Although the adsorption energy of other intermediates (*NO₂, *NO, *N, *NH, *NH₂, *NH₃) on the NiMoO₄ (1 1 3) surface is comparatively lower than that on Cu/Cu₂O (1 1 1) and Cu/CuO (0 0 2), their catalytic performance for nitrate reduction remains limited due to their relatively weak NO₃⁻ Gibbs adsorption energy(-0.49 eV). The experimental and DFT results demonstrate that CuO NW and NiMoO₄ possess excellent catalytic activity towards NO₃⁻-NO₂⁻ and NO₂⁻-NH₃ respectively (**Figure 6e**). During the pre-reduction process, CuO undergoes reduction to form Cu/Cu₂O (Equation 5 and 6). In the NitRR process, a spontaneous redox reaction takes place between Cu/Cu₂O and NO₃⁻, leading to oxidation of Cu/Cu₂O to Cu₂O while reducing NO₃⁻ to NO₂⁻ (Equation 7). Under cathode potential conditions, Cu₂O is reduced back to Cu/Cu₂O for subsequent cycles (Equation 8). H₂O is reduced in the presence of NiMoO₄ to form *H and OH⁻(Equation 9). Additionally, the adsorbed nitrite on the surface of Cu/Cu₂O is gradually converted into NH₃ through interaction with *H generated from NiMoO₄ (Equation 10).



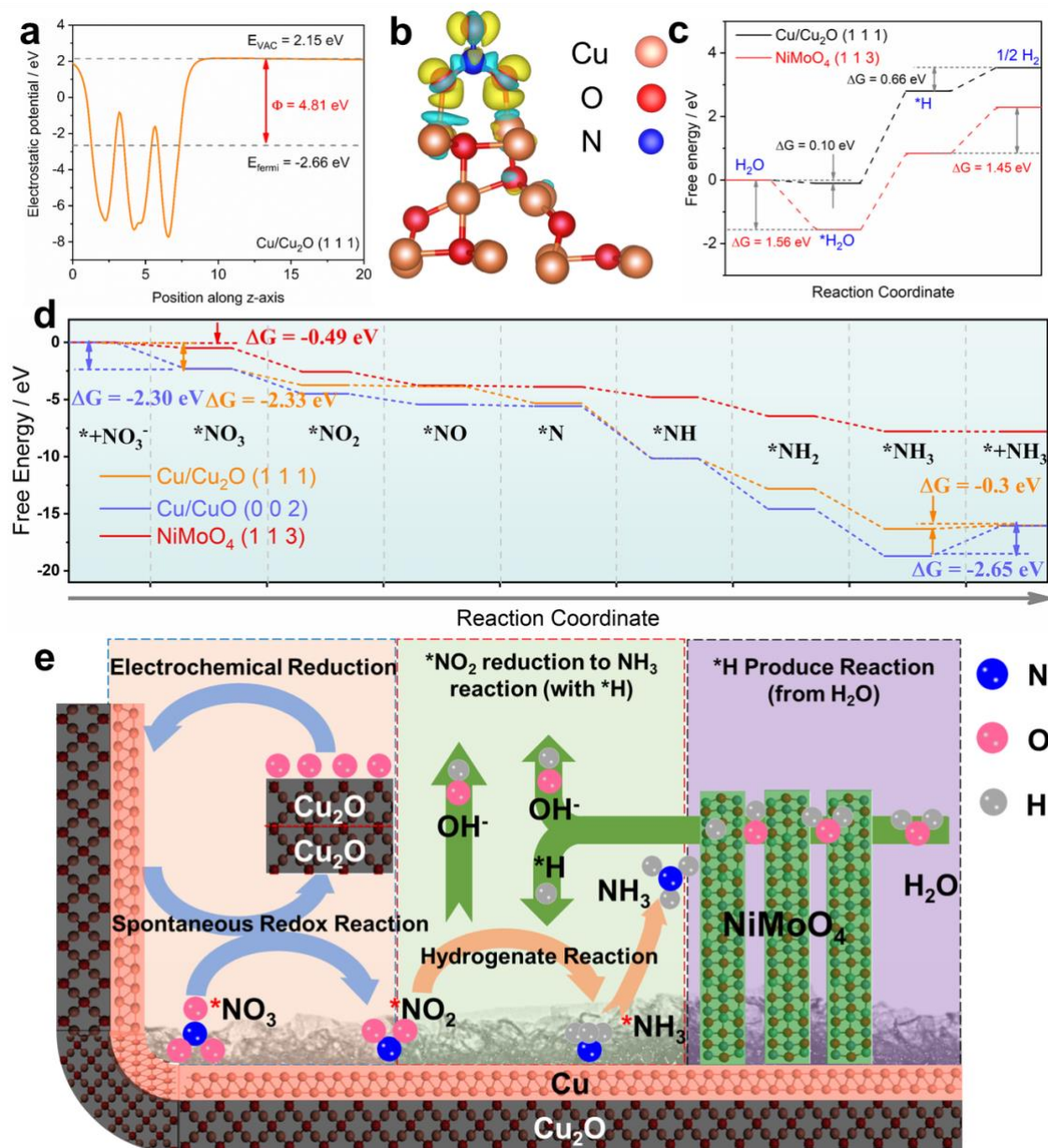
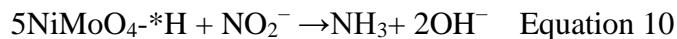
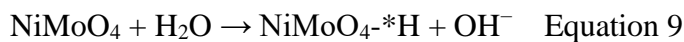
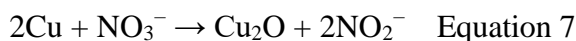
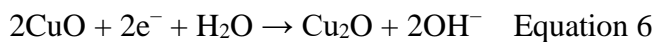


Figure 6 DFT calculations. (a) Electrostatic potentials of Cu/Cu₂O (1 1 1) surface. (b) Charge density difference illustrating *NO₃ adsorption on Cu/Cu₂O (1 1 1) surface. (c) Reaction energies for the adsorption of H₂O and the production of *H and H₂ on Cu₂O (1 1 1) and NiMoO₄ (1 1 3). (d) Calculated Gibbs free energy changes for NitRR leading to NH₃ production at 0 V vs. RHE. (e) Schematic illustration of NiMoO₄-Cu/Cu₂O as NitRR synergistic catalysts.

2.5. Ammonia product collection.

Due to the remarkable performance of NiMoO₄/CuO NW/CF catalyst in NitRR, we further demonstrate its practical application by combining electrocatalysis with air stripping for the continuous collection of high-purity ammonia products (**Figure 7**). The stability of the catalyst at high current densities is crucial for such applications. Initially, we conducted a long-term chrono-potentiometric stability test on NiMoO₄/CuO NW/CF in an H-type cell with continuous electrolyte flow. The potential required to achieve approximately 200 mA cm⁻² on the catalyst remains consistent for 20 hours and remains above 90% NH₃ FE (**Figure 3f**). Due to the elevated ammonia vapor pressure in alkaline environments, we employed air-blowing to efficiently collect ammonia products from wastewater containing NH₃, resulting in over 98.5% removal of generated ammonia from the electrolyte, leaving only 0.83 mg·L⁻¹ and indicating complete denitrification of the water source along with simultaneous generation of valuable ammonia. The stripped ammonia vapor is subsequently trapped in an HCl solution. A significant portion of the outflowing ammonia vapor is captured by the acid solution and after neutralization by NaOH and rotary evaporation, it ultimately forms NH₄Cl (collection efficiency rate of 83.0%) and NaCl powder which serves as fertilizer. XRD analysis confirms the formation of NH₄Cl and NaCl (**Figure 7b**). In summary, we present a comprehensive process that directly converts nitrate-containing feed water into actual ammonia products using our NiMoO₄/CuO NW/CF catalyst.

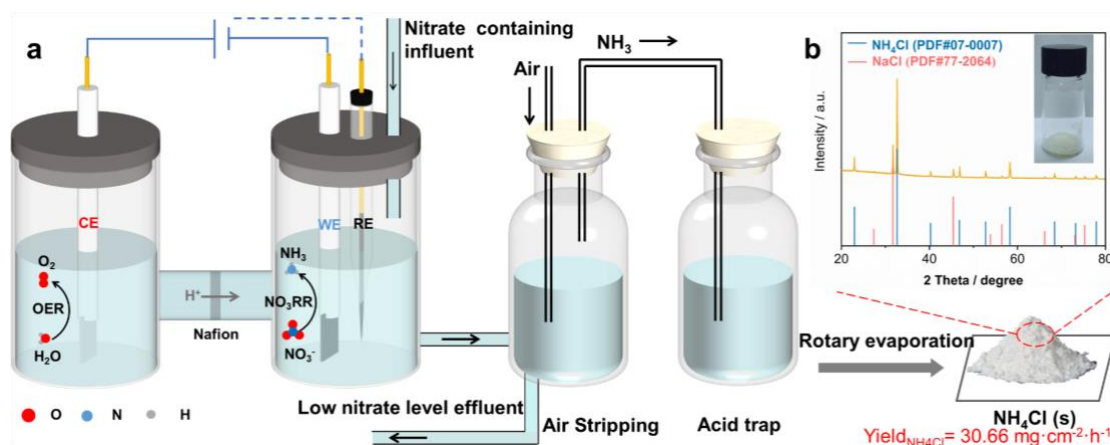


Figure 7 Practical ammonia products synthesis. (a) Schematic of the ammonia product synthesis process from nitrate-containing influent to NH₄Cl(s). (b) Synthesized NH₄Cl products and corresponding XRD patterns.

3. Conclusion

In summary, our hydrothermal synthesis of NiMoO₄ on in-situ-derived Cu nanowire catalysts has demonstrated a high NH₃ Faraday efficiency of 98.8% and yield of 0.8221 mmol h⁻¹ cm⁻² at -0.2 V vs. reversible hydrogen electrode. This system also yielded exceptional stability over a 20-hour period in the NitRR process within the H-type cell. Coupling the nitrate reduction

effluent stream with an air stripping process enabled the efficient collection of NH_4Cl products, presenting a pragmatic solution for transforming wastewater nitrate into valuable ammonia products. Our in-situ electrochemical investigations, coupled with DFT calculations, unveiled the cooperative heterogeneous catalytic effects between $\text{Cu}/\text{Cu}_2\text{O}$ (1 1 1) and NiMoO_4 species as the key contributors to the outstanding NitRR performance. Notably, the preferential adsorption of NO_3^- on $\text{Cu}/\text{Cu}_2\text{O}$ (1 1 1) surface facilitated its conversion to NO_2^- , while the superior hydrogen adsorption capability of NiMoO_4 provided $^*\text{H}$ for subsequent hydrogenation reactions involving N intermediates, ultimately leading to NH_3 production. This study presents a compelling strategy for enhancing NH_3 generation through NitRR and offers profound insights into the reaction mechanism involving copper catalysts activated by $^*\text{H}$ donors.

4. Experimental Section

See the Supporting Information for details of the chemicals and materials, electrode preparation, characterization, electrochemical performance testing, in-situ Raman testing, DFT calculation methods, and performance parameter calculations.

Supporting Information

Supporting Information is available from the Wiley Online Library or from the author.

Acknowledgements

The authors gratefully acknowledge the financial supports from the National Natural Science Foundation of China, the financial support from Cardiff University and the Royal Society IEC\NSFC\211201-International Exchanges 2021 Cost Share (NSFC). The authors thank Jinwen Shi at the State Key Laboratory of Power Engineering multiphase Flow of Xi'an Jiaotong University for their assistance with EPR analysis, Pei Zhou at the Instrument Analysis Center of Xi'an Jiaotong University for their assistance with ^1H NMR analysis.

Conflict of Interest

The authors declare no conflict of interest.

Data Availability Statement

The data that support the findings of this study are available in the supplementary material of this article.

Received: ((will be filled in by the editorial staff))

Revised: ((will be filled in by the editorial staff))

Published online: ((will be filled in by the editorial staff))

References

- [1] V Rosca, M Duca, M T de Groot, M T M Koper, *Chem. Rev.* **2009**, 109, 2209.
- [2] Y Ashida, K Arashiba, K Nakajima, Y Nishibayashi, *Nature* **2019**, 568, 536.
- [3] S L Foster, S I P Bakovic, R D Duda, S Maheshwari, R D Milton, S D Minteer, M J Janik, J N Renner, L F Greenlee, *Nat. Catal.* **2018**, 1, 490.
- [4] R F Service, *Science* **2014**, 345, 610.
- [5] T Kandemir, M E Schuster, A Senyshyn, M Behrens, R Schlögl, *Angew. Chem., Int. Ed.* **2013**, 52, 12723.
- [6] Z-Y Wu, M Karamad, X Yong, Q Huang, D A Cullen, P Zhu, C Xia, Q Xiao, M Shakouri, F-Y Chen, J Y Kim, Y Xia, K Heck, Y Hu, M S Wong, Q Li, I Gates, S Siahrostami, H Wang, *Nat. Commun.* **2021**, 12, 2870.
- [7] X Cui, C Tang, Q Zhang, *Adv. Energy Mater.* **2018**, 8, 1800369.
- [8] J Wang, L Yu, L Hu, G Chen, H Xin, X Feng, *Nat. Commun.* **2018**, 9, 1795.
- [9] P Chen, N Zhang, S Wang, T Zhou, Y Tong, C Ao, W Yan, L Zhang, W Chu, C Wu, Y Xie, *Proc. Natl. Acad. Sci.* **2019**, 116, 6635.
- [10] G-F Chen, X Cao, S Wu, X Zeng, L-X Ding, M Zhu, H Wang, *J. Am. Chem. Soc.* **2017**, 139, 9771.
- [11] S Z Andersen, V Čolić, S Yang, J A Schwalbe, A C Nielander, J M McEnaney, K Enemark-Rasmussen, J G Baker, A R Singh, B A Rohr, M J Statt, S J Blair, S Mezzavilla, J Kibsgaard, P C K Vesborg, M Cargnello, S F Bent, T F Jaramillo, I E L Stephens, J K Nørskov, I Chorkendorff, *Nature* **2019**, 570, 504.
- [12] W Gao, K Xie, J Xie, X Wang, H Zhang, S Chen, H Wang, Z Li, C Li, *Adv. Mater.* **2023**, 35, 2202952.
- [13] Y Guo, R Zhang, S Zhang, Y Zhao, Q Yang, Z Huang, B Dong, C Zhi, *Energy Environ. Sci.* **2021**, 14, 3938.
- [14] W Zhu, F Yao, Q Wu, Q Jiang, J Wang, Z Wang, H Liang, *Energy Environ. Sci.* **2023**, 16, 2483.
- [15] M Xie, S Tang, Z Li, M Wang, Z Jin, P Li, X Zhan, H Zhou, G Yu, *J. Am. Chem. Soc.* **2023**, 145, 13957.
- [16] S Han, H Li, T Li, F Chen, R Yang, Y Yu, B Zhang, *Nat. Catal.* **2023**, 6, 402.
- [17] C L Ford, Y J Park, E M Matson, Z Gordon, A R Fout, *Science* **2016**, 354, 741.
- [18] Y Wang, A Xu, Z Wang, L Huang, J Li, F Li, J Wicks, M Luo, D-H Nam, C-S Tan, Y Ding, J Wu, Y Lum, C-T Dinh, D Sinton, G Zheng, E H Sargent, *J. Am. Chem. Soc.* **2020**, 142, 5702.
- [19] Y Xu, K Ren, T Ren, M Wang, Z Wang, X Li, L Wang, H Wang, *Appl. Catal. B Environ.* **2022**, 306, 121094.
- [20] Y Wang, L Zhang, Y Niu, D Fang, J Wang, Q Su, C Wang, *Green Chem.* **2021**, 23, 7594.
- [21] M Xu, Q Xie, D Duan, Y Zhang, Y Zhou, H Zhou, X Li, Y Wang, P Gao, W Ye, *ChemSusChem* **2022**, 15, e202200231.
- [22] K-H Kim, H Lee, X Huang, J H Choi, C Chen, J K Kang, D O'Hare, *Energy Environ. Sci.* **2023**, 16, 663.
- [23] G-F Chen, Y Yuan, H Jiang, S-Y Ren, L-X Ding, L Ma, T Wu, J Lu, H Wang, *Nat. Energy* **2020**, 5, 605.
- [24] W Wen, P Yan, W Sun, Y Zhou, X-Y Yu, *Adv. Funct. Mater.* **2023**, 33, 2212236.
- [25] H Jiang, G Chen, O Savateev, J Xue, L-X Ding, Z Liang, M Antonietti, H Wang, *Angew. Chem., Int. Ed.* **2023**, 62, e202218717.
- [26] Y Xu, Y Wen, T Ren, H Yu, K Deng, Z Wang, X Li, L Wang, H Wang, *Appl. Catal. B Environ.* **2023**, 320, 121981.

- [27] J Zhou, F Pan, Q Yao, Y Zhu, H Ma, J Niu, J Xie, *Appl. Catal. B Environ.* **2022**, 317, 121811.
- [28] T Feng, J Wang, Y Wang, C Yu, X Zhou, B Xu, K László, F Li, W Zhang, *Chem. Eng. J.* **2022**, 433, 133495.
- [29] C Zhou, J Bai, Y Zhang, J Li, Z Li, P Jiang, F Fang, M Zhou, X Mei, B Zhou, *J. Hazard. Mater.* **2021**, 401, 123232.
- [30] F-Y Chen, Z-Y Wu, S Gupta, D J Rivera, S V Lamberts, S Pecaut, J Y T Kim, P Zhu, Y Z Finfrock, D M Meira, G King, G Gao, W Xu, D A Cullen, H Zhou, Y Han, D E Perea, C L Muhich, H Wang, *Nat. Nanotechnol.* **2022**, 17, 759.
- [31] X Li, P Shen, X Li, D Ma, K Chu, *ACS Nano* **2023**, 17, 1081.
- [32] J Li, G Zhan, J Yang, F Quan, C Mao, Y Liu, B Wang, F Lei, L Li, A W M Chan, L Xu, Y Shi, Y Du, W Hao, P K Wong, J Wang, S-X Dou, L Zhang, J C Yu, *J. Am. Chem. Soc.* **2020**, 142, 7036.
- [33] Y Zhang, X Chen, W Wang, L Yin, J C Crittenden, *Appl. Catal. B Environ.* **2022**, 310, 121346.
- [34] Z Xiao, M Yang, J Wang, Z Xu, S Zhang, A Tang, R Gao, H Yang, *Appl. Catal. B Environ.* **2022**, 303, 120913.
- [35] Y Fu, S Wang, Y Wang, P Wei, J Shao, T Liu, G Wang, X Bao, *Angew. Chem., Int. Ed.* **2023**, 62, e202303327.
- [36] National Center for Biotechnology Information, 2024, <https://pubchem.ncbi.nlm.nih.gov/periodic>.
- [37] R Daiyan, T Tran-Phu, P Kumar, K Iputera, Z Tong, J Leverett, M H A Khan, A Asghar Esmailpour, A Jalili, M Lim, A Tricoli, R-S Liu, X Lu, E Lovell, R Amal, *Energy Environ. Sci.* **2021**, 14, 3588.
- [38] Z-X Ge, T-J Wang, Y Ding, S-B Yin, F-M Li, P Chen, Y Chen, *Adv. Energy Mater.* **2022**, 12, 2103916.
- [39] Y Li, C Wang, L Yang, W Ge, J Shen, Y Zhu, C Li, *Adv. Energy Mater.* **2023**, 14, 2303863.
- [40] Z Gong, X Xiang, W Zhong, C Jia, P Chen, N Zhang, S Zhao, W Liu, Y Chen, Z Lin, *Angew. Chem., Int. Ed.* **2023**, 62, e202308775.
- [41] L Su, K Li, H Zhang, M Fan, D Ying, T Sun, Y Wang, J Jia, *Water Res.* **2017**, 120, 1.
- [42] E Sánchez-Díez, E Ventosa, M Guarnieri, A Trovò, C Flox, R Marcilla, F Soavi, P Mazur, E Aranzabe, R Ferret, *J. Power Sources* **2021**, 481, 228804.
- [43] H Liu, X Lang, C Zhu, J Timoshenko, M Rüscher, L Bai, N Guijarro, H Yin, Y Peng, J Li, Z Liu, W Wang, B R Cuenya, J Luo, *Angew. Chem., Int. Ed.* **2022**, 61, e202202556.
- [44] W Zheng, L Zhu, Z Yan, Z Lin, Z Lei, Y Zhang, H Xu, Z Dang, C Wei, C Feng, *Environ. Sci. Technol.* **2021**, 55, 13231.
- [45] B Xu, Z Chen, G Zhang, Y Wang, *Environ. Sci. Technol.* **2022**, 56, 614.
- [46] J Zhang, W He, T Quast, J R C Junqueira, S Saddeler, S Schulz, W Schuhmann, *Angew. Chem., Int. Ed.* **2022**, 135, e202214830.
- [47] G Solomon, A Landström, R Mazzaro, M Jugovac, P Moras, E Cattaruzza, V Morandi, I Concina, A Vomiero, *Adv. Energy Mater.* **2021**, 11, 2101324.
- [48] W Du, Y Shi, W Zhou, Y Yu, B Zhang, *Angew. Chem., Int. Ed.* **2021**, 60, 7051.
- [49] W He, S Chandra, T Quast, S Varhade, S Dieckhöfer, J R C Junqueira, H Gao, S Seisel, W Schuhmann, *Adv. Mater.* **2023**, 62, 2303050.
- [50] D Yin, D Chen, Y Zhang, W Wang, Q Quan, W Wang, Y Meng, Z Lai, Z Yang, S Yip, C-Y Wong, X Bu, X Wang, J C Ho, *Adv. Funct. Mater.* **2023**, DOI: <https://doi.org/10.1002/adfm.2023038032303803>.
- [51] M Xu, F Wu, Y Zhang, Y Yao, G Zhu, X Li, L Chen, G Jia, X Wu, Y Huang, P Gao, W Ye, *Nat. Commun.* **2023**, 14, 6994.

Table of Contents

NiMoO₄ loaded on Cu₂O/Cu displays efficient NitRR performance towards ambient NH₃ synthesis in alkaline medium. An innovative strategy is proposed, utilizing Cu₂O/Cu and NiMoO₄ as synergistic heterogeneous catalysts, significantly increasing the selectivity and FE of NH₃.

C. Lin, X. Chen, L. Wang, W. Li, Z. Wang, M. Li, J. Feng,* B. Hou,* and W. Yan,*

Electrocatalytic Conversion of Nitrate into Ammonia through Heterogeneous Catalysis of NiMoO₄ and Cu/Cu₂O

